Broadband Optical Detection Using the Spin Seebeck Effect

Subash Kattel,[1] Joseph R. Murphy,[1] David Ellsworth,[2] Jinjun Ding,[2] Tao Liu,[2] Peng Li,[2]
Mingzhong Wu,[2] and William D. Rice[1],[*]

[1] *Department of Physics and Astronomy, University of Wyoming, Laramie, Wyoming 82071, USA*
[2] *Department of Physics, Colorado State University, Fort Collins, Colorado 80523, USA*

The generation, control, and detection of spin currents in solid-state devices are critical for Joule-heating minimization, spin-based computation, and electrical-energy generation from thermal gradients. Although incorporation of spin functionality into technologically important architectures is still in its infancy, advantages over all-electric devices are increasingly becoming clear. Here, we utilize the spin Seebeck effect (SSE) in $Pt/Y_3Fe_5O_{12}$ devices to detect light from 390 to 2200 nm. We find that the device responsivity is remarkably flat across this technologically important wavelength range, closely following the Pt absorption coefficient. As expected from a SSE-generation mechanism, we observe that the photovoltage and Pt heating dynamics are in strong agreement. To precisely determine the optically created thermal gradient produced from a pointlike heat source, we introduce a field-modulation method for measuring the SSE. Our results show that broadband optical detection can be performed with devices based solely on spin-current generation and detection.

I. INTRODUCTION

Spin-current generation, detection, transport, and manipulation are key components of a new generation of spin-based devices that have both spin and electrical characteristics [1,2]. Unlike traditional all-electrical devices, these architectures utilize a flow of spins (i.e., a spin current density, $\mathbf{J}_s$) to transmit information and/or energy in lieu of the carrier charge [3,4]. Given the weak interactions between most types of matter and carrier spins, pure spin currents transmit energy significantly more efficiently than charge currents, which unavoidably incur energetic losses in nonsuperconducting materials. However, the magnetic nature of spin also means that its incorporation into traditional charge-based devices remains a technologically significant hurdle. Moreover, it continues to be unclear that utilizing the carrier spin (instead of their charge) actually produces a marked performance enhancement in device performance except in selected cases, such as giant magnetoresistance, or in magneto-optical devices [5].

To explore the advantages that pure spin currents (i.e., a net spin flow without net charge movement) may have over traditional optoelectronics, researchers have focused on three main ways to create $\mathbf{J}_s$: the spin Seebeck effect (SSE) [6], spin pumping [7,8], and the spin Hall effect [1,9–11]. In particular, the SSE has gained substantial attention in the past few years as a way to convert thermal energy to electrical energy (i.e., spin caloritronics) [12]. Like the electrical Seebeck effect, in which a thermal gradient, ∇T, produces a current density in materials with itinerant charge carriers [13], the SSE occurs when a thermal gradient produces a pure spin current. However, unlike its electrical analog, the SSE has been generated not just in ferromagnetic metals [6] and semiconductors [14], but also in magnetic insulators [15–17].

Beyond these three main pure-spin-current generation mechanisms, recent work by Ellsworth *et al.* [18] has suggested a fourth pure-spin-current-generation pathway called the photo-spin-voltaic (PSV) effect [19], which produces $\mathbf{J}_s$ from the unequal dephasing of spin-polarized photogenerated electrons and holes in Pt. Unlike the other pure-spin-current-generation mechanisms, the PSV effect occurs in the nonmagnetic metal top layer and has only been observed via optical excitation. Given that both the longitudinal SSE (LSSE) and the PSV effect are ultimately measured via a voltage across the nonmagnetic metal top layer, the all-optical nature of the PSV effect makes its empirical signatures difficult to distinguish from the optically generated LSSE. Although a spin-current density can be generated in a wide variety of magnetic materials through the aforementioned mechanisms, measuring it primarily relies on either the inverse spin Hall effect (ISHE) [7,8,20,21], which produces an electrical voltage from a spin current via spin-orbit coupling, or polarization-sensitive optical detection, which utilizes out-of-plane magnetization to alter the incoming light polarization [22–24].

*wrice2@uwyo.edu

In this work, we utilize the bulk SSE in $Pt/Y_3Fe_5O_{12}$ (YIG) bilayer devices to detect light from 390 to 2200 nm, demonstrating that pure-spin-current generation can be used for broadband optical detection. We show that the spin-current-generated ISHE voltage, V_{ISHE}, is nearly featureless over this ultrabroadband optical range, with a responsivity, $\mathcal{R}(\lambda)$, which follows the absorption coefficient of Pt. In contrast to previous work [18], we find that the dynamical response of the device closely matches the thermal behavior of Pt, which suggests that the SSE is the underlying detection mechanism. Finally, we introduce an amplitude-modulated technique for SSE detection, which we use to measure ∇T due to the optical heating from the Pt film. From our determination of ∇T, along with the measured ISHE voltage gradient, we estimate the LSSE coefficient, $S_{LSSE} (= V_{ISHE}/\nabla T)$, for this Pt/YIG configuration to be 60 ± 7.8 nV/K. These results suggest that featureless broadband photodetection can be readily achieved by thermally generated spin currents, thus avoiding spectrally limited photocarrier creation in semiconductors and showing strong similarities to thermoelectric photodetectors.

II. RESULTS AND DISCUSSION

In this work, we use bilayer devices prepared using the procedure described in Ellsworth *et al.* [18]. Briefly, a layer of YIG is grown via liquid-phase epitaxy on a $Gd_3Ga_5O_{12}$ (GGG) substrate with a thickness of either 80 nm or 15 μm, depending on the sample series. Next, radio-frequency magnetron sputtering overcoats the YIG with Pt. The Pt/YIG devices have a Pt film thickness, t_{Pt}, ranging from 2 to 6 nm; a diagram of this heterostructure is shown in Fig. 1(a). In the first Pt/YIG/GGG device series (YIG thickness = 15 μm), the 500-μm-thick GGG is polished only on the side on which the YIG layer is deposited; in the second device set (YIG thickness = 80 nm), the GGG substrate is polished on both sides, which allows optical excitation from either face of the device.

Figure 1(b) schematically shows the experimental setup used to obtain the majority of the results in this work. The measurements are conducted in the LSSE geometry [15,21], whereby a uniform magnetic field is applied in the plane of the device perpendicular to the optically induced ∇T, creating a J_s that is proportional to the local YIG magnetization, **M**. As will be shown later, we use the ISHE to detect J_s, which creates a spin-dependent transverse electric field that is orthogonal to both ∇T and **M** [21]. The exact origin of the LSSE, either from a thermal gradient across the YIG [15] (bulk SSE) or a difference of interfacial temperatures between the Pt and YIG [23] (interfacial SSE), cannot be unambiguously determined from either experimental technique that we use in this paper; however, as shown later, we are very likely observing the bulk LSSE.
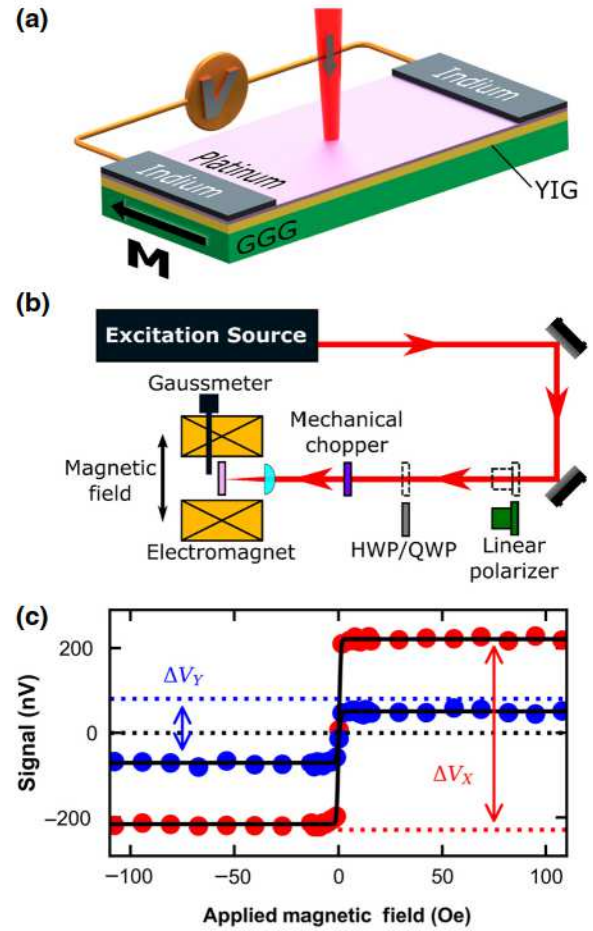

FIG. 1. The Pt/YIG device layout and photovoltage measurement. (a) The nonmagnetic metal (Pt)/magnetic insulator (YIG) bilayer structure on GGG. For a given device, the thickness of the Pt metal layer ranges from 2 to 6 nm. A magnetic field is applied perpendicular to the incident light direction, producing an in-plane YIG magnetization, **M**. (b) A schematic of the experimental setup used to collect the steady-state excitation signal. Depending on the experiment, a linear polarizer and either a half-wave plate (HWP) or a quarter-wave plate (QWP) are added to the optical excitation path. (c) The field-dependent in- and out-of-phase signals, V_X and V_Y, respectively, measured using a lock-in amplifier. The solid lines are error-function fits to the data.

Although the LSSE geometry is straightforward to implement, its configuration and our use of thin Pt (< 10 nm) allows other mechanisms, such as the anomalous Nernst effect [25] and magnetic proximity effects [26], to occur. However, previous work done using directional magnetization [27] and Pt/Cu/YIG and Au/Cu/YIG structures [28] strongly suggests that the LSSE dominates these effects in Pt/YIG bilayers.

We measure the optically generated V_{ISHE} between two pressed-indium contacts using a lock-in amplifier (LIA) triggered by an optical chopper. The resulting signal from a standard field sweep (-100 to $+100$ Oe) and the

corresponding error-function fit are shown in Fig. 1(c). We clearly observe that as the field is swept, the device voltage rapidly rises from negative to positive values between -30 and $+30$ Oe, reflecting the change in the YIG magnetization. We call the in-phase difference in signal level between opposite field directions ΔV_X, which is defined as $[V_{X,H_+} - V_{X,H_-}] \approx 2V_{X,H_+} \approx 2V_{X,H_-}$ [21,29]; the asymmetry in the field-dependent signal that is sometimes observed ($V_{X,H_+} \neq V_{X,H_-}$) is related to an unintentional tilt of the device in the field. $\frac{1}{2}\Delta V_X$ is reported as the device signal throughout this work, except for the last experiment.

A. Detection via the inverse spin Hall effect

In distinct contrast to photoconductivity, where optically generated carriers produce a measurable voltage (or current), and optical thermoelectricity, in which a photoinduced thermal gradient produces a voltage via the (electrical) Seebeck effect, we *only* observe a photovoltage in the presence of a (small) magnetic field. As demonstrated in Fig. 1(c), the steady-state voltage obtained at higher applied fields shows that the YIG must be fully magnetized in order to achieve full device responsivity [15]. More precise information can be gleaned if we pair how the signal varies as a function of the field with its angular dependence. Specifically, if we are indeed using the ISHE to detect spin currents, then rotating the magnetic field direction and thus the spin polarization vector, σ, will change the electric field generated between the two contacts, $\mathbf{E}_{\mathrm{ISHE}}$ [8,15]:

$$-\nabla V_{\mathrm{ISHE}} = \mathbf{E}_{\mathrm{ISHE}} = \frac{1}{\sigma_c}D_{\mathrm{ISHE}}(\mathbf{J}_s \times \sigma), \quad (1)$$

where σ_c is the electrical conductivity ($\mathbf{E}_{\mathrm{ISHE}} = \frac{1}{\sigma_c}\mathbf{J}_c$), and D_{ISHE} is the ISHE coefficient.

To measure this field-angle dependence in Eq. 1, we place the Pt/YIG bilayer device between the poles of an electromagnet that has the ability to rotate a full 360° around the bilayer detector (Fig. 2). For each angle of the electromagnet, θ, taken with respect to the $\hat{x}$ axis, the magnetic field is scanned from -100 Oe to $+100$ Oe. The field scan at each angle is then fitted with an error function, from which the signal is determined.

Figure 2 shows the magnitude of the resulting signal from this field sweep as a function of θ. The normalized signal clearly follows a sinusoidal pattern (black fit line), which corresponds to σ rotating from orthogonal to $\mathbf{E}_{\mathrm{ISHE}}$ (maximum magnitude) to parallel with it (zero magnitude) and is consistent with previous works utilizing pure spin-current detection via the ISHE [8,15,18,30]. Importantly, the use of the magnetic field vector to observe a photovoltage from a Pt-based device demonstrates how spin currents can create functionality and distinguishes these measurements from a photoconductive effect in either Pt or YIG.
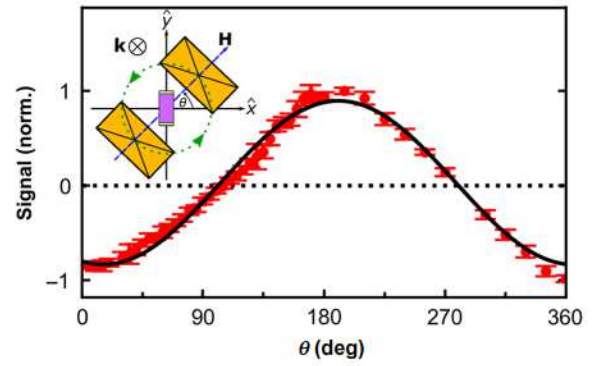

FIG. 2. As the direction of the magnetic field is rotated with respect to the bilayer device, the variation of the (normalized) signal exhibits a sinusoidal pattern (black fit line), which agrees well with previous ISHE observations. Inset: a graphical depiction of the rotational field dependence experiment. The electromagnets (orange) are rotated a full 360° about the bilayer device. With the indium contacts aligned along the $\hat{y}$ axis, θ is defined as the angle between the applied magnetic field, $\mathbf{H}$, and the $\hat{x}$ axis. The incident light, the direction of which is defined by the $\mathbf{k}$ vector, is set in the $-\hat{z}$ orientation.

B. Spectral response of the Pt/YIG devices

The initial findings of Ellsworth and coworkers [18] suggested that the spectral dependence of these bilayer systems may help to determine the primary spin-current-generation mechanism: that is, to distinguish between the SSE and the PSV effect. To measure the device spectral response, we use a wide variety of illumination sources, which necessitate examining how the Pt/YIG devices respond to different light polarizations, incident powers, and pulse repetition rates. The upper panel of Fig. 3(a) shows that the voltage signal is constant when the linear polarization is rotated via a half-wave plate (HWP) over 360°. Similarly, despite the strong spin-orbit coupling of Pt [20], the device signal remains unchanged when the ellipticity of the light polarization is tuned from linear to circular with a quarter-wave plate (QWP). The lack of polarization dependence is significant not just from a technological point of view, but it also enables our implementation of the double-sided illumination experiment discussed later.

To compare the device response obtained at different wavelengths, we need to verify that we can normalize the signal by the incident power. In Fig. 3(b), we find that the signal scales linearly for several different wavelengths. This linearity allows us to define a device responsivity, $\mathcal{R}$, for a given wavelength, λ: $\mathcal{R}(\lambda) = V_{\mathrm{ISHE}}(\lambda)/P_{\mathrm{incident}}(\lambda)$, where $P_{\mathrm{incident}}(\lambda)$ is the incident power at λ. Figure 3(c) presents the measured $\mathcal{R}$ as a function of the incident power across over 4 orders of magnitude for the 2-nm-thick Pt device. Despite the large change in incident power, the responsivity drop is less than a factor of 100, which compares favorably with power-dependent $\mathcal{R}$ trends in
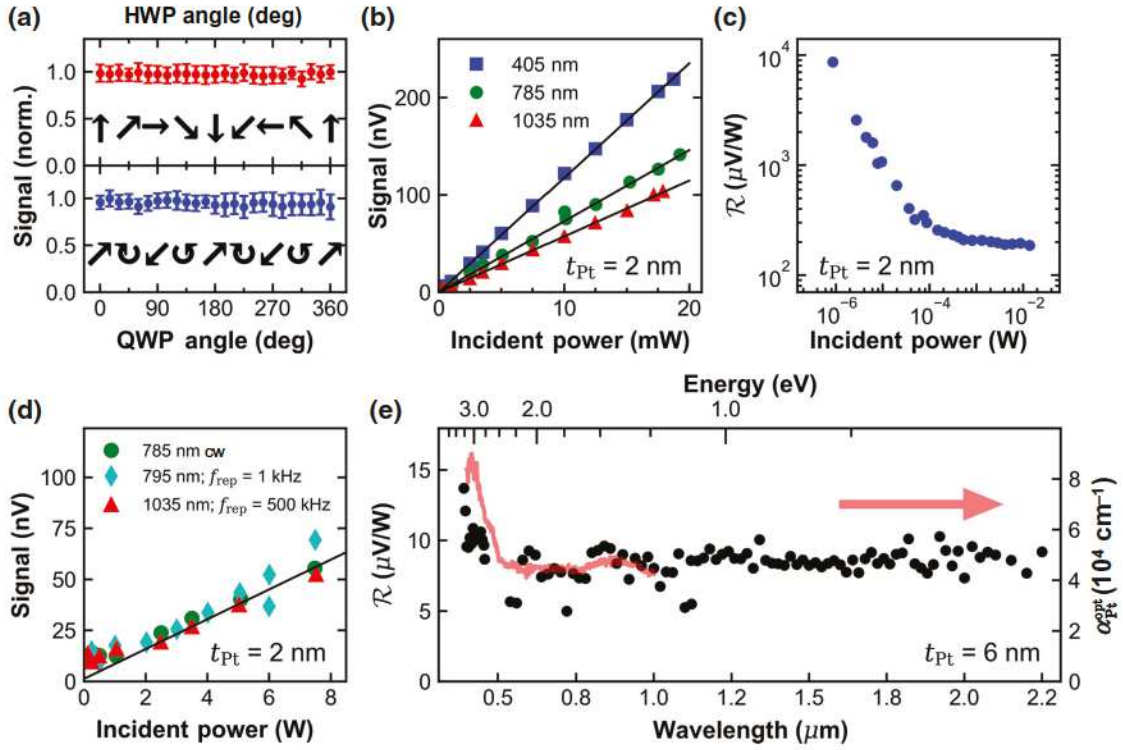
FIG. 3. The optical response of the Pt/YIG device. (a) In the upper panel, the normalized V_{ISHE} produced by the incident light shows no change as the linear polarization (HWP) angle is rotated. Similarly, in the lower panel, we observe no change when the light polarization is changed via rotation of a QWP. (b) The signal power dependence for three wavelengths shows a linear scaling, which allows us to normalize the signal by the incident power (i.e., the device responsivity). The magnitude of the signal from a 405-nm excitation is clearly larger than the signals from excitation wavelengths of 785 nm and 1035 nm. (c) The device responsivity, $\mathcal{R}(\lambda)$, as a function of the incident power for 405 nm on a 2-nm-thick Pt/YIG device. (d) The voltage signal created by illumination from different pulsed (795 nm, 1 kHz repetition rate, pulse duration approximately 180 fs; 1035 nm, 500 kHz repetition rate, pulse duration approximately 220 fs) and cw sources as a function of the average power. Regardless of the repetition rate, the device signal linearly scales with the average incident power. (e) $\mathcal{R}(\lambda)$ from 390 to 2200 nm (black dots) for the 6-nm-thick Pt/YIG device. The responsivity is remarkably flat from 450 to 2200 nm with a small increase of $\mathcal{R}$ below 450 nm. This spectral trend closely follows the measured absorption coefficient of the Pt film (red).

recent experimental device structures, such as black phosphorous carbide [31] and graphene heterostructures [32].

Figure 3(d) shows the power-dependent voltage response from excitation sources with different pulse repetition rates. We find that as the repetition rate of the laser is varied from continuous wave (cw) to 1 to 500 kHz (pulse duration approximately 200 fs for both pulsed excitation sources), the device response is exactly the same. This behavior suggests that the mechanism for generating a photovoltage is based on thermal effects, since the signal only depends on the average incident power. We note that previous researchers have shown spin accumulation times for Pt/YIG structures on the order of 10^{-12} to 10^{-11} s [23] and for magnon dynamics on the order of 10^{-7} s [29], which occur on much faster time scales than the data shown here. Importantly, the similarity of the observed response when the device is excited with either cw or ultrafast pulsed light (including at different repetition rates) as a function of the average power strongly suggests that the

interfacial SSE, which has been shown to occur between the Pt and YIG on time scales of tens of picoseconds [23], is not influencing our steady-state observations; based on this (indirect) evidence, we believe that the bulk SSE is the dominant mechanism here.

The spectral dependence of the device responsivity from 390 to 2200 nm is obtained using several different excitation sources. In the ultraviolet region, from 390 to 460 nm, a frequency-doubled, Ti:sapphire oscillator is used, while in the visible and near-infrared regimes (540–2200 nm), we utilize a combination of second-harmonic generation, sum-frequency generation, and signal and/or idler beams from a Ti:sapphire-pumped, optical parametric amplifier (OPA). Finally, we confirm the near-infrared results using a tunable-wavelength, Ti:sapphire oscillator from 760 to 990 nm.

To ensure that this broadband spectral dependence is accurate, we use significant filtering to eliminate spurious spectral components from the illumination sources.

This operation is especially critical for the OPA output, which contains multiple output wavelengths due to the nature of the optical-generation mechanisms. Given the polarization dependence of the various frequency-mixing operations (sum-frequency, difference-frequency, and second-harmonic generation), we direct the OPA output through two linear polarizers to remove significant fractions of nonrelevant wavelengths, which is then followed by a set of dielectric and elemental filters (e.g., germanium for near-infrared light) to further isolate the desired λ. To ensure the spectral purity of the incident light, we pass the light through a Princeton Instruments SP2150 monochromator and perform a lock-in amplifier-based scan using a single-channel InGaAs detector. These spectral scans are done at every other excitation wavelength above 1100 nm.

Figure 3(e) shows the spectral dependence of $\mathcal{R}(\lambda)$ for the 6-nm-thick Pt/YIG device spanning from 390 to 2200 nm, the limits of our optical excitation range. In contrast to the PSV effect predictions [18] and semiconductor-based photodetectors, the measured spectral responsivity is nearly *featureless*: we observe no significant changes in the value of $\mathcal{R}(\lambda)$ or sign flips. The red curve in Fig. 3(e) displays the measured optical absorption coefficient, α_{Pt}^{opt}, from 390 to 1000 nm of the 6-nm-thick Pt layer. The matching spectral dependencies of both $\mathcal{R}(\lambda)$ and α_{Pt}^{opt} strongly suggest that the absorption of the Pt is central to the observed behavior.

The unexpectedly flat and broadband spectral responsivity of our devices represents a remarkable improvement, both in spectral uniformity and range, over traditional semiconductor-based photodetectors, as well as more exotic configurations claiming ultrabroadband responsivities, such as few-layer black phosphorous [33], ferroelectric-gated MoS_2 [34], MoS_2-graphene-WSe_2 heterostructures [32], graphene heterostructures [35], and nanotube-graphene hybrids [36]. The extension of the device spectral range deep into the near infrared (and possibly much farther) opens up the possibility for using this type of architecture for converting thermal radiation into electrical energy, similar to demonstrations of spin-based thermoelectrics [12]. Unlike photodetectors based on photovoltage, photogating, plasmon, or cavity enhancement [37], or carrier multiplication and/or avalanching, in which either the carrier population or the carrier mobility is (optically) changed, our device has more in common with the broad spectral responsivities seen in thermally based detection mechanisms, such as photothermoelectrics, thermopiles, pyroelectrics, and bolometers, in which the device conductance is altered via the lattice temperature. However, unlike these more traditional mechanisms in which the semiconductor carrier mobility or metallic and/or superconductor conductivity is altered by an optically created temperature increase, our detection mechanism relies on the optical generation and electrical detection of spin currents. This fundamentally different photodetection process is advantageous, because it leverages materials with high absorptivity (e.g., heavy metals) that do not create easily recoverable carriers, while also avoiding the lossy process of carrier separation, injection, and recovery. Although we note that the magnitude of our measured $\mathcal{R}(\lambda)$ remains well below that of more optimized, photocarrier-based architectures [35,36], recent work on improving the SSE efficiency [38,39] shows that much larger values of $\mathcal{R}(\lambda)$ are achievable in spin caloritronic devices.

C. Influence of the platinum-layer thickness on the device responsivity

Although the Pt film is the thinnest part of the bilayer structure (thinner, in fact, than the estimated Pt skin depth of approximately 11 nm in this wavelength range), the large absorption coefficient ($\alpha_{Pt}^{opt} \sim 10^5$ cm^{-1}) is the dominant per unit length absorption contribution in the system. As mentioned above, we use Pt/YIG bilayers with varying t_{Pt} to generalize our observations. Given that total absorption increases linearly with t_{Pt}, a naive expectation is that V_{ISHE} and $\mathcal{R}$ follows this same dependence.

Figure 4(a) shows V_{ISHE} as a function of the incident power for all three Pt film thicknesses. It is immediately clear that a monotonic increase photovoltage is observed with decreasing t_{Pt}. A plot of $\mathcal{R}$ as a function of t_{Pt} in
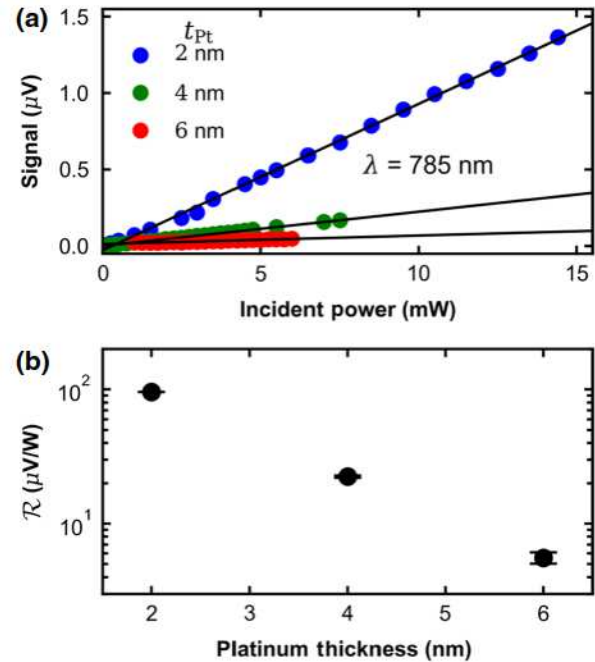

FIG. 4. (a) The SSE signal at 785 nm scales linearly with the incident power for different Pt film thicknesses, t_{Pt}. (b) The responsivity, $\mathcal{R}(\lambda = 785$ nm), as a function of the Pt film thickness. For the three Pt thicknesses measured, we see that as t_{Pt} decreases, $\mathcal{R}$ increases significantly.

Fig. [4(b)] indicates that the device responsivity drops by over an order of magnitude when the Pt film thickness is increased from 2 to 6 nm. Follow-on measurements of $\mathcal{R}(\lambda)$ from 390 to 1600 nm on the 4-nm-thick Pt/YIG device show that this Pt thickness scaling holds across a broad range of wavelengths. These results suggest that the energy absorbed per unit length, which is proportional to α_{Pt}^{opt}, and the proximity to the YIG layer are two critical parameters for determining $\mathcal{R}$. Nevertheless, it is still surprising that as the thickness is increased from 2 to 6 nm, $\mathcal{R}$ drops by over an order of magnitude. Previous work on changing t_{Pt} in Pt/YIG bilayers [40], as well as theoretical models of how S_{SSE} varies with Pt thickness, show that as t_{Pt} decreases, S_{SSE} increases. However, the significant decrease of $\mathcal{R}$ with increasing t_{Pt} may be affected via other factors, such as spin scattering at the Pt/YIG interface, differences in Pt film wetting on the YIG [41], thermal gradients across the Pt film [42], differences in the effective absorption coefficient of the Pt [42], interfacial Rashba spin-orbit interactions, and thickness-dependent spin-diffusion lengths. Further investigation of how $\mathcal{R}$ depends on t_{Pt} is ongoing.

D. Conditions on the photovoltage generation

In the previous sections, the importance of the Pt layer in the operation of the device is firmly established, while the role of the GGG and, in particular, heating effects related to its absorption of light, remain unexplored. In this section, we isolate the role of the GGG by either altering the excitation geometry or manipulating the Pt layer.

To see if we can produce a thermal gradient across the YIG via some manner other than illuminating the Pt top layer, we attempt to directly optically heat the GGG substrate. In the first experiment, the GGG substrate is excited from the back side of the bilayer with the goal of flipping the sign of ∇T. While keeping the total photon number fixed, the percentage of the total power incident on the front and back is continuously varied by means of a HWP and a polarization-selective Glan-Taylor polarizer in front of a beam splitter. Although the incident light polarization states on the front and back sides of the device are different in this geometry, we show in Fig. [3(a)] that V_{ISHE} is polarization insensitive. Figure [5(a)] demonstrates that as the incident power illumination is shifted, the $\mathcal{R}$ only changes slightly. The insignificant difference with the illumination
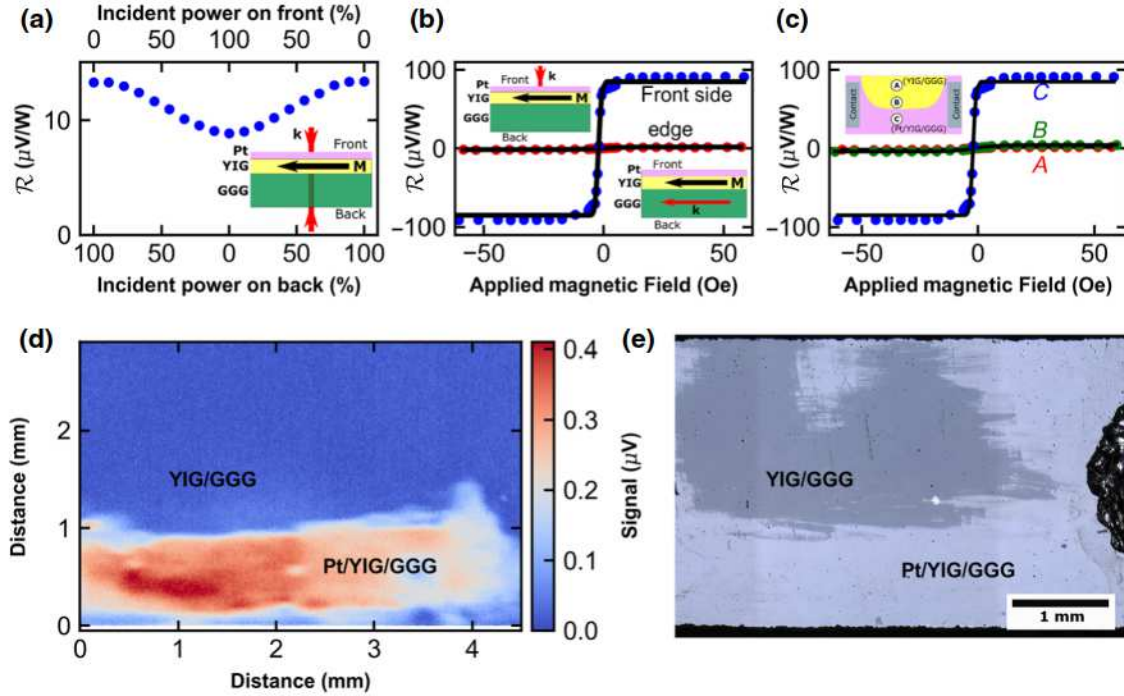

FIG. 5. (a) The device responsivity as optical excitation is varied between the front and back of the device. Since the sign of $\mathcal{R}(\lambda)$ does not change when the illumination direction is switched from the front to the back, we conclude that the optically generated thermal gradient remains the same regardless of the illumination orientation. (b) When a 785-nm diode laser is incident on the front side of the 2-nm-thick Pt/YIG device (blue), a large signal is observed. In contrast, when this beam at the same power is incident on the GGG only (from the side; red), a very small voltage signal is obtained. (c) The signal obtained by illuminating Pt/YIG/GGG (blue) and two different locations (red and green) on YIG/GGG with the Pt top layer removed. The solid black lines are fits to data. The top left inset shows the illumination spot on the sample in a region with (represented by C) and without the Pt layer (A and B). (d) Two-dimensional (2D) mapping of the voltage signal, showing variation across a sample with partially removed Pt areas. (e) An optical image of the sample where the signal mapping in (c) is performed.

direction suggests that the GGG (and YIG) is not absorbing a substantial amount of light per unit length [21,43,44]. If it is, ∇T across the YIG will flip signs, thus reversing the direction of $\mathbf{J}_s$ and inverting the sign of V_{ISHE}.

As a follow-on to this experiment, we directly illuminate the GGG from the side of the device ("edge illumination") using different excitation sources (405- and 785-nm diode lasers). Since the front side of the device is at room temperature (i.e., a cold Pt-YIG interface), we are again interested in seeing if the temperature rise of the GGG reverses the thermal gradient across the YIG and flips the sign of V_{ISHE}. However, this time, we avoid any illumination of the Pt film in an attempt to better distinguish between the PSV effect (which requires Pt optical excitation) and the SSE.

To perform the edge-illumination experiment, we use diamond-grit abrasive paper to polish the two opposite sides of the device, which minimizes optical scattering. As the edges are lapped, we monitor the surface quality and device integrity using an optical microscope. Light is directed through the entire length of the GGG, thus optically heating only the bottom of the YIG via the hot GGG. Figure 5(b) clearly shows that the signal obtained during edge illumination is very small when compared to front-side illumination with the same excitation power. Taken together, these two direct GGG optical excitation results show that either (1) the ∇T ($\propto V_{ISHE}$) across the YIG is dominated by optical heating of the Pt layer and contributions from the GGG substrate are negligible or (2) the PSV effect is actually the dominant spin-current generation mechanism instead of the SSE.

In addition to optical heating of the YIG top layer via the nanometer-thick Pt film, we find that a strong photocreated signal also requires that the Pt film remain continuous and connected to the contacts. To demonstrate this condition, we mechanically remove half of the Pt film from the 2-nm-thick Pt/YIG device using a plastic spatula. An optical microscope is used to monitor the removal process, to avoid damaging the device. We perform a point-by-point scan of the half-Pt device using a three-axis stage, which is automated for three-axis movement, and a long-working-distance microscope objective (Mitutoyu NIR 50×) with a measured spot size of 20 μm. We scan an area of 3.3 mm × 4.5 mm with a step size of 5 μm, using an excitation wavelength of 785 nm; at each location, V_{ISHE} is measured via a lock-in amplifier locked to a mechanical chopper modulating the light intensity. Although 785 nm is outside the higher-absorption regions of YIG and GGG, we observe a similar behavior (with single-location excitation) using a 405-nm laser. After confirming the V_{ISHE} signal with a magnetic field sweep at a fixed location, the static applied field is set at 100 Oe, and the device is moved in a 2D pattern.

Figure 5(d) shows the result of this scan, with the regions indicated in red corresponding to the highest level of signal. In direct comparison to this SSE signal map, an optical image of the same total area is shown in Fig. 5(e). The region that corresponds to the highest signal in the 2D signal map is the region in which the Pt film remains continuous between the two indium contacts. As expected, the device generates a voltage when the optical beam illuminates a region of intact Pt. Interestingly, however, we do not see an appreciable signal when the optical excitation is on Pt regions that are disconnected from the indium contacts. This observation, along with the measured field-angle dependence of V_{ISHE} (Fig. 4) [8,15], confirms that we are using the ISHE to detect spin currents. However, despite the substantial amount of data presented thus far, we still cannot *conclusively* determine whether the SSE and/or PSV effect is the dominant spin-current generation mechanism.

E. Thermal response dynamics

In order to help distinguish between the PSV effect and the SSE, we measure the temporal device response and compare it to the temperature dynamics of the Pt layer. As shown earlier in Fig. 3(d), the magnitude and (average) power scaling of V_{ISHE} do not change when the optical illumination is changed from a continuous excitation to various pulsed sources, which suggests that the signal is generated from a purely thermal heating mechanism. A more direct measurement of this hypothesis is given in Fig. 6(a), which shows the signal response (red) of four, light-on–light-off cycles over the course of approximately 85 s. When the light is unblocked, the device immediately (to within our instrument resolution of 10 ms) generates a voltage, which is consistent with results obtained by Ellsworth and coworkers [18] using a broadband source. However, unlike these previous results, the *thermal* response of the Pt to the light exactly follows the signal response. Both this rapid temperature rise and equilibration of the Pt layer temperature and its strong agreement with the device response suggest that we are observing the SSE rather than a photocarrier-mediated process.

A deeper insight into the SSE mechanism in these devices can be obtained by determining the magnitude of the Pt temperature change created by the optical beam. This estimate necessitates determining the temperature coefficient of resistance for the Pt film, α_{Pt}^{TC}, which is used in the relation for the temperature-dependent resistance, $R(T)$ [45]: $R(T) = R_0[1 + \alpha^{TC}(T - T_0)]$, where R_0 is the resistance at a known temperature T_0. In Fig. 6(b), we show the change of R as a function of the temperature to obtain $\alpha_{Pt}^{TC} = (2.39 \pm 0.01) \times 10^{-4}$ K^{-1} = $0.0736\,(5)\,\alpha_{Pt}^{TC\,bulk}$. The discrepancy between the bulk Pt temperature coefficient, $\alpha_{Pt}^{TC\,bulk}$ [45,46], and the measured temperature coefficient of our thin Pt layers, α_{Pt}^{TC}, is attributable to the incomplete and fragmented nature of metallic films when the thickness is on the order of
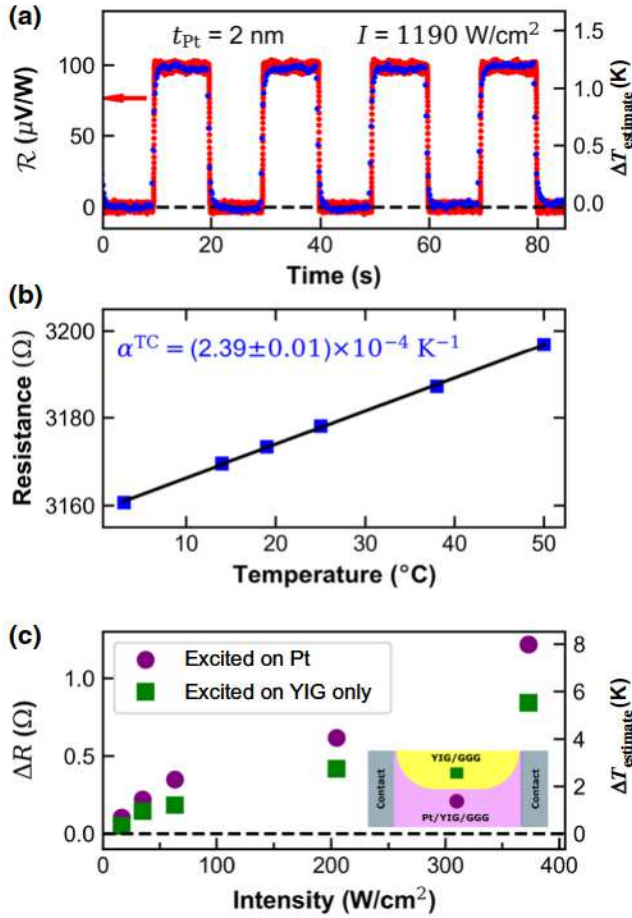
FIG. 6. (a) The device responsivity (red dots) with illumination off and on in 20-s intervals. The device response is faster than the measurement time resolution (10 ms; see the right-hand vertical axis). The estimated temperature change (blue dots), $\Delta T_{estimate}$, of the Pt film using the measured value for α_{Pt}^{TC} during the off-on illumination cycles. The dynamics (within our resolution) of the power-normalized signal and the bulk-resistivity change to the optical excitation are the same. (b) The increase in the resistance of the Pt film with the temperature. The black solid line is the linear fit to the data. The measured value of the temperature coefficient, α_{Pt}^{TC}, is found to be 2.39×10^{-4} K^{-1} when illuminated with 1190 W/cm^2 using a 405-nm laser as the excitation source. (c) The Pt-layer temperature rise (right y axis), $\Delta T_{estimate}$, can be estimated from the change in the Pt resistance, ΔR. As indicated by the inset, we illuminate on (purple dots) and off (green squares) the Pt/YIG bilayer.

nanometers [47]. Using this lower value for α_{Pt}^{TC}, we find that the estimated Pt-film temperature rise, $\Delta T_{estimate}$, created by an optical intensity of 1190 W/cm^2 is approximately 1.5 K. If we assume the temperature of the bottom side of the YIG to be unchanged by the optical beam (as we have empirically shown earlier), then the approximately 1.5 K change in the Pt film is actually an estimate of ΔT across the YIG, a value that is large enough for the observation of a small SSE signal. Despite the efforts

we take to determine ΔT from directly measuring the ΔR of the Pt layer, this estimate is not very accurate in our particular case for two reasons: (1) the optical illumination is over only a fraction of the total Pt layer; and (2) the optical beam has a Gaussian profile. In both cases, we are deviating substantially from the situation of an evenly heated bulk slab of Pt, which is intrinsically assumed in our calculation of $\Delta T_{estimate}$.

Additionally, we also measure the change in the Pt temperature when the YIG/GGG is optically illuminated. In this experiment, we measure the Pt temperature as a function of the optical power when the beam is on and off of the Pt. Although we do not observe an appreciable V_{ISHE} from the YIG/GGG illumination (Fig. 5), we do measure a significant temperature change of the *adjacent* Pt top layer, as shown in Fig. 6(c). This temperature rise indicates that the thermal energy from the absorbed light diffuses through the YIG/GGG, but not sufficiently enough to create a ∇T that produces a non-negligible V_{ISHE}.

F. Amplitude-modulation detection of the spin Seebeck effect

To resolve uncertainty in the determination of ΔT, we modify our experiment to *unambiguously* detect the SSE, as well as to precisely measure ∇T. In the reconfigured experimental setup, which is shown in Fig. 7(a), the device is mounted on a copper heat sink, which is thermally mated to a thermoelectric cooler (TEC). As before, a magnetic field is perpendicular to both the incoming light and the long axis of the device. However, instead of modulating the optical intensity and sweeping the magnetic field, we remove the chopper and add a slow (13.1 Hz) and small ($\simeq 1$ G) field modulation, H_1, to the larger, sweeping applied field, H_0. By locking onto this modulation frequency, we obtain a voltage signal that corresponds to the derivative of the device response. The key advantage of measuring this amplitude-modulated (AM) signal is that it allows us to study the SSE with or without light.

The left-hand panel in Fig. 7(b) shows the AM signal as a function of the copper-heat-sink temperature, T_{Cu}. As discussed previously, the SSE occurs when ∇T is established across the YIG in the presence of H_0. In our case, $\nabla T \simeq (T_{Pt} - T_{GGG})/L_{YIG}$, where T_{Pt} and T_{GGG} are close approximations of the top- and bottom-side temperatures, respectively, of the YIG and L_{YIG} is the YIG thickness. For the light-off measurements, we assume that T_{Pt} is at room temperature (approximately 20 °C). Consequently, as we increase T_{Cu} (approximately T_{GGG}) from 4 to 50 °C, ∇T correspondingly goes from positive through zero to negative, which is reflected in the magnitude and sign of the field-scanned AM signal. The addition of a 1190-W/cm^2-intensity beam at 405 nm increases T_{Pt} and thus shifts ∇T by a fixed amount. The right panel of Fig. 7(b) shows this behavior exactly: the point at which the AM signal is zero
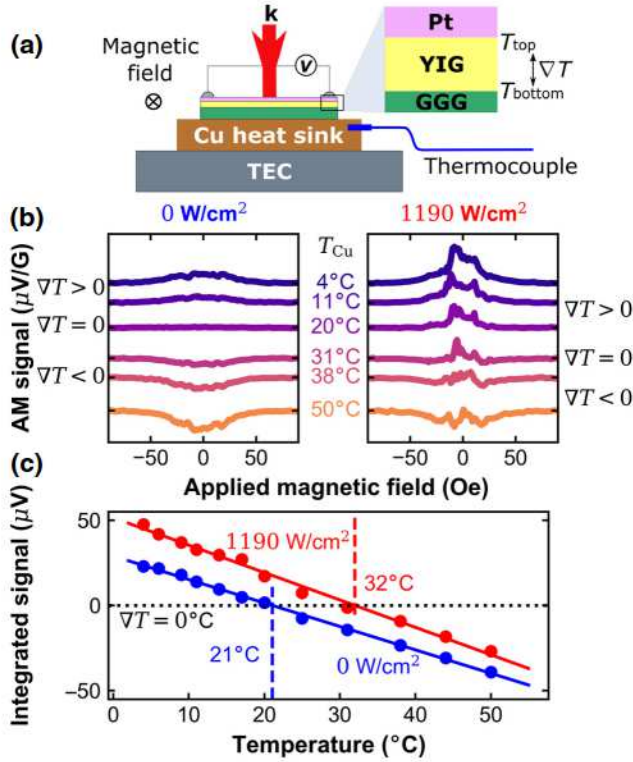
FIG. 7. Measurement of the SSE using a field amplitude-modulation technique. (a) The Pt/YIG/GGG device mounted on a copper heat sink attached to a TEC for back-side temperature control. (b) The amplitude-modulated (AM) signal with different copper-heat-sink temperatures, T_{Cu}, with (right) and without (left) optical illumination. As T_{Cu} is increased, the temperature gradient across the YIG, ∇T, goes from negative to positive, which is mirrored by the sign of the AM signal. (c) The integrated AM signal with (red) and without (blue) optical illumination. The shift of approximately 11 K is created by the Pt absorption of the light and is directly attributable to the SSE.

for the light-on condition occurs when T_{Cu} is at a larger value. We note that more advanced modeling is necessary for an exact determination of ∇T under optical excitation, especially since the temperature across the Pt film is not constant [42].

Given that the AM signal is proportional to the derivative of the optical-modulation signal, the integration of the curves shown in Fig. 7(b) is comparable to the SSE signal discussed in previous sections. Figure 7(c) shows the integrated SSE AM signal as a function of T_{Cu} for both the light off (blue) and on (red). Since $V_{ISHE} \propto J_s^{SSE} \propto \nabla T \simeq [T_{Pt} - T_{GGG}] (1/L_{YIG}) \simeq [T_{Pt} - T_{Cu}] (1/L_{YIG})$, the key point here is that the integrated AM signal is proportional to the magnitude and sign of the SSE-generated spin-current density, J_s^{SSE}. Critically, the difference between the light-on and -off curves is in fact a highly accurate (relative) measure of the thermal heating due to optical illumination; that is, the only thing changing between the curves shown in Fig. 7(c) is the presence of an additional

(optical) heating source. This relative comparison removes the inaccuracies incurred by thickness-dependent temperature gradients across the Pt film [42] and sample-specific properties [41]. Taking the point at which both curves cross zero ($\nabla T \simeq 0$), we find that when compared to the light-off condition, the optically created temperature difference between the top and bottom sides of the YIG is approximately 11 K using an intensity of 1190 W/cm². This temperature difference due to the light, as well as the lack of heating due to optical absorption by the GGG substrate (Fig. 5), suggests that we can accurately determine the optically created thermal gradient across the 15-μm-thick YIG to be $\nabla T \simeq \frac{\Delta T}{L_{YIG}} = 0.73$ K/μm. Furthermore, we know that this intensity generates a V_{ISHE} of 3.457 μV across the approximately 80-μm beam spot size, which is roughly measured by two indium contacts spaced 4.45 mm apart, giving $E_{ISHE} = -\nabla V_{ISHE} = 3.457$ μV/80 μm = 43 mV/m. Using our estimates for ∇T and $-\nabla V_{ISHE}$, we calculate a quantity akin to a traditional Seebeck coefficient for S_{LSSE} in this Pt/YIG device: $|S_{LSSE}| = |-\nabla V_{ISHE}/\nabla T| = 60 \pm 7.8$ nV/K. This estimate is in line with previous measurements of S_{LSSE} in Pt/YIG heterostructures [38,39,48,49], but orders of magnitude below (electrical) Seebeck coefficients found in thermoelectric devices [50,51].

On the basis of spectral, dynamic, and field-modulated measurements, we believe that the observed V_{ISHE} is created via a spin current produced from the (optically heated) bulk SSE. This interpretation does not exclude the possibility that the PSV effect [18] may also be present here. However, a calculation using the estimated number of optically generated carriers in Pt for the powers that we use in these experiments (details given in Appendix B), suggests that any PSV signal should be, at maximum, approximately 4.9 nV. Given that the measured V_{ISHE} is on the order of 10^{-6} V, any PSV effect is likely negligible. Moreover, the extremely flat, broadband, but low responsivity correlates well with (electrical) Seebeck effect devices, such as thermopiles.

III. CONCLUSIONS

Taken together, our results show a spin-based detection of broadband light across the Si-InGaAs detection range. The spectral responsivity from 390 to 2200 nm is attributed to Pt absorption, which creates a spin current from the SSE. We find that ∇T across the underlying YIG layer from the incident light used to produce this spin current is 0.73 K/μm; this thermal gradient measurement allows us to estimate $|S_{LSSE}|$ to be $\simeq 60$ nV/K. Unlike previous optical detectors that are fully reliant on charge carriers, the devices that we examine here use spin current to produce a voltage response from light. Our measurements of an ultrabroadband and featureless $\mathcal{R}(\lambda)$, combined with previous SSE dynamical studies [23,29] and routes for

enhancing S_{LSSE} [38,39], suggest the promise of a spin-based optical detector that is competitive with current photovoltage architectures.

APPENDIX A: TEMPERATURE-CHANGE ESTIMATION USING THE RESISTANCE OF PLATINUM

The resistance of the optically illuminated Pt is directly measured as a function of the optical power to ascertain $\alpha_{\mathrm{Pt}}^{\mathrm{TC}}$, the resistance temperature coefficient. Changes in temperature, ΔT, are related to resistance changes via the following [45]:

$$\Delta T = \frac{\Delta R}{R_0}\frac{1}{\alpha_{\mathrm{Pt}}^{\mathrm{TC}}}, \qquad (A1)$$

where ΔR is the change in the resistance and R_0 is the resistance under no optical illumination. From the data shown in Fig. 6(b), we determine $\alpha_{\mathrm{Pt}}^{\mathrm{TC}}$ to be 2.39×10^{-4} K^{-1}, which is significantly smaller than the α^{TC} of bulk Pt, which is equal to 3.92×10^{-3} K^{-1} [46].

APPENDIX B: MAGNITUDE OF THE PHOTO-SPIN-VOLTAIC EFFECT

Ellsworth *et al.* [18] have suggested that spin-polarized photogenerated carriers created in Pt and oriented via proximity to a magnetized insulator (in our case, YIG) can produce voltage signals similar to the ones that we observe. In order to distinguish our results from the PSV effect, we estimate the magnitude from a 405-nm laser with an incident power of 18 mW and a beam diameter of 80 μm, giving an intensity, I, of 3.6 MW/m^2. Starting with Eq. 1, we recognize that D_{ISHE} is equal to $-\theta_{\mathrm{SH}}(2e/\hbar)$, where θ_{SH} is the spin Hall angle and has been reported to range from 10^{-4} to 10^0 [6,20,30,52]. Since the charge-current density, $\mathbf{J}_c$, equals $\sigma_c \mathbf{E}_{\mathrm{ISHE}}$, where σ_c is measured to be $\sigma_c = 7.07 \times 10^5$ S/m, we can estimate the magnitude of ΔV_{ISHE} as follows:

$$\Delta V_{\mathrm{ISHE}} = \theta_{\mathrm{SH}}\left(\frac{2e\ell}{\hbar\sigma_c}\right)J_s, \qquad (B1)$$

where ℓ ($= 4.45 \times 10^{-3}$ m) is the measured distance between the indium contacts.

Next, we estimate the magnitude of $\mathbf{J}_s$ created by the incident light. In the model put forth by Ellsworth and coworkers [18], the electron spin density, J_s^e, is approximately zero, which means that the hole spin density, J_s^h, becomes the only contribution to J_s. Thus, for the spin-current density, we have [18] $J_s^h = J_s = -\frac{1}{2}E_{\mathrm{light}}d_0 t_{\mathrm{Pt}}(\epsilon_\uparrow'' - \epsilon_\downarrow'')$. Here, E_{light} is the electric field of the light and d_0 is the region of Pt affected by the magnetization of the YIG, which we take to be 1 Å, reflecting the small extent of the proximity effect. It is only in this region that optically generated holes and electrons are spin polarized, which means that we only need to consider optical absorption within this thickness. As such, the light electric field in the ferromagnetic Pt region, $z_{\mathrm{FM}} = t_{\mathrm{Pt}} - d_0$, is: $E_{\mathrm{light}}(z_{\mathrm{FM}}) = e^{-\frac{\alpha}{2}z_{\mathrm{FM}}}\sqrt{\frac{2I}{c\epsilon_0}}$, where $\alpha_{\mathrm{Pt}}^{\mathrm{opt}}$ ($\simeq 10^7$ m^{-1}) is the measured Pt absorption coefficient, c is the speed of light, and ϵ_0 is the vacuum permittivity. We can therefore relate the light intensity to the magnitude of the hole spin density:

$$J_s = \frac{1}{2}E_{\mathrm{light}}(z_{\mathrm{FM}})d_0 t_{\mathrm{Pt}}(\epsilon_\uparrow'' - \epsilon_\downarrow''). \qquad (B2)$$

Using Eqs. (B1) and (B2), the relationship between the magnitude of ΔV_{ISHE} and I for the PSV effect can thus be written as follows:

$$\Delta V_{\mathrm{ISHE}} = \theta_{\mathrm{SH}}\left(\frac{e\ell d_0 t_{\mathrm{Pt}}}{\hbar\sigma_c}\right)e^{-\frac{\alpha}{2}z_{\mathrm{FM}}}\sqrt{\frac{2I}{c\epsilon_0}}(\epsilon_\uparrow'' - \epsilon_\downarrow''). \qquad (B3)$$

For our estimate, we take $\theta_{\mathrm{SH}} = 10^{-1}$ [30] and $\epsilon_\uparrow'' - \epsilon_\downarrow'' \approx 0.5$ [18]. Plugging in these numbers, we can find that ΔV_{ISHE} for our 2-nm-thick Pt device to be approximately 4.9 nV, which is 3 orders of magnitude smaller than the observed signal, 3.457 μV, at this wavelength and optical intensity. Although the predicted wavelength dependence of $(\epsilon_\uparrow'' - \epsilon_\downarrow'')$ changes from positive to negative, its expected magnitude never goes above 5 (that is, a factor of 10 below what we used in this estimate for 405 nm). Increasing *both* θ_{SH} and $\epsilon_\uparrow'' - \epsilon_\downarrow''$ by an order of magnitude still puts us a factor of 10 below our empirical observations. Thus, given the size of the estimated PSV effect signal for these intensities, as well as the lack of wavelength dependence observed in our measurements, we believe that the V_{ISHE} measured in our work comes predominantly from the bulk SSE.

[1] T. Jungwirth, J. Wunderlich, and K. Olejník, Spin Hall effect devices, Nat. Mater. **11**, 382 (2012).

[2] G. E. W. Bauer, E. Saitoh, and B. J. van Wees, Spin caloritronics, Nat. Mater. **11**, 391 (2012).

[3] S. A. Wolf, D. D. Awschalom, R. A. Buhrman, J. M. Daughton, S. von Molnar, M. L. Roukes, A. Y. Chtchelkanova, and D. M. Treger, Spintronics: A spin-based electronics vision for the future, Science **294**, 1488 (2001).

[4] I. Žutić, J. Fabian, and S. Das Sarma, Spintronics: Fundamentals and applications, Rev. Mod. Phys. **76**, 323 (2004).

[5] B. Náfrádi, P. Szirmai, M. Spina, H. Lee, O. V. Yazyev, A. Arakcheeva, D. Chernyshov, M. Gibert, L. Forró, and E. Horváth, Optically switched magnetism in photovoltaic perovskite $CH_3NH_3(Mn:Pb)I_3$, Nat. Comm. **7**, 13406 (2016).

[6] K. Uchida, S. Takahashi, K. Harii, J. Ieda, W. Koshibae, K. Ando, S. Maekawa, and E. Saitoh, Observation of the spin Seebeck effect, Nature **455**, 778 (2008).

[7] A. Azevedo, L. H. Vilela Leão, R. L. Rodriguez-Suarez, A. B. Oliveira, and S. M. Rezende, dc effect in ferromagnetic resonance: Evidence of the spin-pumping effect?, J. Appl. Phys. **97**, 10C715 (2005).

[8] E. Saitoh, M. Ueda, H. Miyajima, and G. Tatara, Conversion of spin current into charge current at room temperature: Inverse spin-Hall effect, Appl. Phys. Lett. **88**, 182509 (2006).

[9] J. E. Hirsch, Spin Hall Effect, Phys. Rev. Lett. **83**, 1834 (1999).

[10] Y. K. Kato, R. C. Myers, A. C. Gossard, and D. D. Awschalom, Observation of the spin Hall effect in semiconductors, Science **306**, 1910 (2004).

[11] S. O. Valenzuela and M. Tinkham, Direct electronic measurement of the spin Hall effect, Nature **442**, 176 (2006).

[12] A. Kirihara, K. Uchida, Y. Kajiwara, M. Ishida, Y. Nakamura, T. Manako, E. Saitoh, and S. Yorozu, Spin-current-driven thermoelectric coating, Nat. Mater. **11**, 686 (2012).

[13] K. Uchida, T. Ota, H. Adachi, J. Xiao, T. Nonaka, Y. Kajiwara, G. E. W. Bauer, S. Maekawa, and E. Saitoh, Thermal spin pumping and magnon-phonon-mediated spin-Seebeck effect, J. Appl. Phys. **111**, 103903 (2012).

[14] C. M. Jaworski, J. Yang, S. Mack, D. D. Awschalom, J. P. Heremans, and R. C. Myers, Observation of the spin-Seebeck effect in a ferromagnetic semiconductor, Nat. Mater. **9**, 898 (2010).

[15] K. Uchida, H. Adachi, T. Ota, H. Nakayama, S. Maekawa, and E. Saitoh, Observation of longitudinal spin-Seebeck effect in magnetic insulators, Appl. Phys. Lett. **97**, 172505 (2010).

[16] K. Uchida, T. Nonaka, T. Ota, and E. Saitoh, Longitudinal spin-Seebeck effect in sintered polycrystalline, $(Mn, Zn)Fe_2O_4$, Appl. Phys. Lett. **97**, 262504 (2010).

[17] K. Uchida, J. Xiao, H. Adachi, J. Ohe, S. Takahashi, J. Ieda, T. Ota, Y. Kajiwara, H. Umezawa, H. Kawai, G. E. W. Bauer, S. Maekawa, and E. Saitoh, Spin Seebeck insulator, Nat. Mater. **9**, 894 (2010).

[18] D. Ellsworth, L. Lei, J. Lan, H. Chang, P. Li, Z. Wang, J. Hu, B. Johnson, Y. Bian, J. Xiao, R. Wu, and M. Wu, Photo-spin-voltaic effect, Nat. Phys. **12**, 861 (2016).

[19] I. Žutić and J. Fabian, Spin-voltaic effect and its implications, Mater. Trans. **44**, 2062 (2003).

[20] T. Kimura, Y. Otani, T. Sato, S. Takahashi, and S. Maekawa, Room-Temperature Reversible Spin Hall Effect, Phys. Rev. Lett. **98**, 156601 (2007).

[21] J. M. Bartell, C. L. Jermain, S. V. Aradhya, J. T. Brangham, F. Yang, D. C. Ralph, and G. D. Fuchs, Imaging Magnetization Structure and Dynamics in Ultrathin $Y_3Fe_5O_12$/Pt Bilayers with High Sensitivity Using the Time-Resolved Longitudinal Spin Seebeck Effect, Phys. Rev. Appl. **7**, 044004 (2017).

[22] G-M. Choi, B.-C. Min, K.-J. Lee, and D. G. Cahill, Spin current generated by thermally driven ultrafast demagnetization, Nat. Comm. **5**, 4334 (2014).

[23] J. Kimling, G.-M. Choi, J. T. Brangham, T. Matalla-Wagner, T. Huebner, T. Kuschel, F. Yang, and D. G. Cahill, Picosecond Spin Seebeck Effect, Phys. Rev. Lett. **118**, 057201 (2017).

[24] R. McLaughlin, D. Sun, C. Zhang, M. Groesbeck, and Z. V. Vardeny, Optical detection of transverse spin-Seebeck effect in permalloy film using sagnac interferometer microscopy, Phys. Rev. B **95**, 180401(R) (2017).

[25] A. Sakai, Y. P. Mizuta, A. A. Nugroho, R. Sihombing, T. Koretsune, M.-T. Suzuki, N. Takemori, R. Ishii, D. Nishio-Hamane, R. Arita, P. Goswami, and S. Nakatsuji, Giant anomalous Nernst effect and quantum-critical scaling in a ferromagnetic semimetal, Nat. Phys. **14**, 1119 (2016).

[26] S. Y. Huang, X. Fan, D. Qu, Y. P. Chen, W. G. Wang, J. Wu, T. Y. Chen, J. Q. Xiao, and C. L. Chien, Transport Magnetic Proximity Effects in Platinum, Phys. Rev. Lett. **109**, 107204 (2012).

[27] T. Kikkawa, K. Uchida, S. Daimon, Y. Shiomi, H. Adachi, Z. Qui, D. Hou, X.-F. Jin, S. Maekawa, and E. Saitoh, Separation of longitudinal spin Seebeck effect from anomalous Nernst effect: Determination of origin of transverse thermoelectric voltage in metal/insulator junctions, Phys. Rev. B **88**, 214403 (2013).

[28] B. F. Miao, S. Y. Huang, D. Qu, and C. L. Chien, Absence of anomalous Nernst effect in spin Seebeck effect of Pt/YIG, AIP Adv. **6**, 015018 (2016).

[29] M. Agrawal, V. I. Vasyuchka, A. A. Serga, A. Kirihara, P. Pirro, T. Langer, M. B. Jungfleisch, A. V. Chumak, E. Th. Papioannou, and B. Hillebrands, Role of bulk-magnon transport in the temporal evolution of the longitudinal spin-Seebeck effect, Phys. Rev. B **89**, 224414 (2014).

[30] H. L. Wang, C. H. Du, Y. Pu, R. Adur, P. C. Hammel, and F. Y. Yang, Scaling of Spin Hall Angle in 3d, 4d, and 5d Metals $Y_3Fe_5O_{12}$/metal Spin Pumping, Phys. Rev. Lett. **112**, 197201 (2014).

[31] W. C. Tan, L. Huang, R. J. Ng, L. Wang, D. M. N. Hasan, T. J. Duffin, K. S. Kumar, C. A. Nijhuis, C. Lee, and K.-W. Ang, A black phosphorus carbide infrared phototransistor, Adv. Mater. **30**, 1705039 (2018).

[32] M. Long et al., Broadband photovoltaic detectors based on an atomically thin heterostructure, Nano Lett. **16**, 2254 (2016).

[33] M. Buscema, D. J. Groenendijk, S. I. Blanter, G. A. Steele, H. S. J. van der Zant, and A. Castellanos-Gomez, Fast and broadband photoresponse of few-layer black phosphorous field-effect transistors, Nano Lett. **14**, 3347 (2014).

[34] X. Wang, P. Wang, J. Wang, W. Hu, X. Zhou, N. Guo, H. Huang, S. Sun, H. Shen, T. Lin, M. Tang, L. Liao, A. Jiang, J. Sun, X. Meng, X. Chen, W. Lu, and J. Chu,

Ultrasensitive and broadband MoS_2 photodetector driven by ferroelectrics, Adv. Mater. **27**, 6575 (2015).

[35] C-H. Liu, Y.-C. Chang, T. B. Norris, and Z. Zhong, Graphene photodetectors with ultra-broadband and high responsivity at room temperature, Nat. Nanotech. **9**, 273 (2014).

[36] Y. Liu, F. Wang, X. Wang, X. Wang, E. Flahaut, X. Liu, Y. Li, X. Wang, Y. Xu, Y. Shi, and R. Zhang, Planar carbon nanotube-graphene hybrid films for high-performance broadband photodetectors, Nat. Comm. **6**, 8589 (2015).

[37] D. A. Bandurin, D. Svintsov, I. Gayduchenko, S. G. Xu, A. Principi, M. Moskotin, I. Tretyakov, D. Yagodkin, S. Zhukov, T. Taniguchi, K. Watanabe, I. V. Grigorieva, M. Polini, G. N. Goltsman, A. K. Geim, and G. Fedorov, Resonant terahertz detection using graphene plasmons, Nat. Comm. **9**, 5392 (2018).

[38] H. Yuasa, F. Nakata, R. Nakamura, and Y. Kurokawa, Spin Seebeck coefficient enhancement by using Ta_5W_{50} alloy and YIG/Ru interface, J. Phys. D: Appl. Phys. **51**, 134002 (2018).

[39] F. Nakata, T. Niimura, Y. Kurokawa, and H. Yuasa, Spin Seebeck voltage enhancement by Mn system metals insertion at the interface between YIG and nonmagnetic layer, Jpn. J. Appl. Phys. **58**, SBBI04 (2019).

[40] M. Weiler, M. Althammer, M. Schreier, J. Lotze, M. Pernpeintner, S. Meyer, H. Huebl, R. Gross, A. Kamra, J. Xiao, Y.-T. Chen, H. Jiao, G. E. W. Bauer, and S. T. B. Goennenwein, Experimental Test of the Spin Mixing Interface Conductivity Concept, Phys. Rev. Lett. **111**, 176601 (2013).

[41] A. Aqeel, I. J. Vera-Marun, B. J. van Wees, and T. T. M. Palstra, Surface sensitivity of the spin Seebeck effect, J. Appl. Phys. **116**, 153705 (2014).

[42] S. Surabhi, D.-J. Kim, P. C. Van, V. D. Quoc, J.-K. Kim, S. W. Lee, R. Kuchi, J.-W. Lee, S.-G. Yoon, J. Choi, B.-G. Park, and J.-R. Jeong, Precise determination of the temperature gradients in laser-irradiated ultrathin magnetic layers for the analysis of thermal spin current, Sci. Rep. **8**, 11337 (2018).

[43] G. B. Scott and J. L. Page, The absorption spectra of $Y_3Fe_5O_12$ and $Y_3Ga_5O_12$: Fe^{3+} to 5.5 eV, Phys. Stat. Sol. (b) **79**, 203 (1977).

[44] M. A. Ellabban, M. Fally, R. A. Rupp, and L. Kovács, Light-induced phase and amplitude gratings in centrosymmetric gadolinium gallium garnet doped with calcium, Opt. Express **14**, 593 (2006).

[45] J. Zhang, Y. Nagao, S. Kuwano, and Y. Ito, Microstructure and temperature coefficient of resistance of platinum films, Jpn. J. Appl. Phys. **36**, 834 (1997).

[46] W. F. Gale and T. C. Totemeier, in *Smithells Metals Reference Book 8th edition* (Elsevier, 2004), p. 14-1.

[47] Y. Namba, Resistivity and temperature coefficient of thin metal films with rough surface, Jpn. J. Appl. Phys. **9**, 1326 (1970).

[48] A. Sola, M. Kuepferling, V. Basso, M. Pasquale, T. Kikkawa, K. Uchida, and E. Saitoh, Evaluation of thermal gradients in longitudinal spin Seebeck effect measurements, J. Appl. Phys. **117**, 17C510 (2015).

[49] A. Sola, P. Bougiatioti, M. Kuepferling, D. Meier, G. Reiss, M. Pasquale, T. Kuschel, and V. Basso, Longitudinal spin Seebeck coefficient: Heat flux vs. temperature difference method, Sci. Rep. **7**, 46752 (2017).

[50] A. I. Boukai, Y. Bunimovich, J. Tahir-Kheli, J.-K. Yu, W. A. Goddard III, and J. R. Heath, Silicon nanowires as efficient thermoelectric materials, Nature **451**, 168 (2008).

[51] T. Ye, X. Wang, X. Li, A. Q. Yan, S. Ramakrishna, and J. Xu, Ultra-high Seebeck coefficient and low thermal conductivity of a centimeter-sized perovskite single crystal acquired by a modified fast growth method, J. Mater. Chem. C **5**, 1255 (2017).

[52] T. Seki, Y. Hasegawa, S. Mitani, S. Takahashi, H. Imamura, S. Maekawa, J. Nitta, and K. Takanashi, Giant spin Hall effect in perpendicularly spin-polarized FePt/Au devices, Nat. Mater. **7**, 125 (2008).